Point-by-Point model calculation of the prompt neutron multiplicity distribution $\nu(A)$ for ^{238}U(n,f) at incident neutron energies ranging from 1 MeV to 80 MeV

A. Tudora,[1,*] F.-J. Hambsch,[2] and V. Tobosaru[1]

[1]*Faculty of Physics, University of Bucharest, Bucharest Magurele, 405 Atomistilor Street, POB MG-11, R0-77125, Romania*

[2]*EC-JRC Institute for Reference Materials and Measurements (IRMM), Retieseweg 111, B-2440 Geel, Belgium*

(Received 9 March 2016; revised manuscript received 28 June 2016; published 4 October 2016)

Prompt neutron multiplicity distributions $\nu(A)$ are generally required for prompt emission correction of double energy ($2E$) measurements of fission fragments in order to determine pre-neutron fragment properties. The lack of experimental $\nu(A)$ data especially at higher incident neutron energy imposes the use of prompt emission models to predict $\nu(A)$. At incident neutron energies (En) where multiple fission chances are involved, the Point-by-Point (PbP) model of prompt emission is able to provide the individual $\nu(A)$ of the compound nuclei of the main and secondary nucleus chains that are undergoing fission at a given En. The total $\nu(A)$ are obtained by averaging these individual $\nu(A)$ over the fission chance probabilities (expressed as total and partial fission cross-section ratios). An indirect validation of the total $\nu(A)$ results is proposed. At high En (above 70 MeV) the PbP results of individual $\nu(A)$ of the first few nuclei of the main and secondary nucleus chains exhibit an almost linear increase. This shape is explained by the damping of shell effects entering the superfluid expression of the level-density parameters. They tend to approach the asymptotic values for a great part of the fragments. This fact leads to a smooth and almost linear increase of fragment excitation energy with the fragment mass number that is reflected in a smooth and almost linear behavior of individual $\nu(A)$. The comparison of the present results with those of the GEF code reveals different shapes of $\nu(A)$ as well as different total average neutron multiplicity as a function of the En. At high En the PbP calculations definitely reflect the influence of the almost linear shape of individual $\nu(A)$ of the first few nuclei of the U and Pa chains. The differences between the total $\nu(A)$ obtained by averaging the PbP results of individual $\nu(A)$ over fission cross-section ratios of different evaluations are insignificant.

DOI: 10.1103/PhysRevC.94.044601

I. INTRODUCTION

Although many experimental and theoretical investigations in the nuclear fission field were performed during the past decades, the evolution of fission fragment observables with increasing incident neutron energy (En) is not yet well understood. Albeit experimental information about proton-induced fission at intermediate energies exist, for neutron-induced fission the data are very scarce, almost inexistent. Nowadays there is an interest in the study of neutron-induced fission at intermediate and high energies, justified by the need of nuclear data for both advancing of our understanding of the fission process and new applications, e.g., advanced nuclear systems based on fission, incineration of nuclear waste, isotope production, etc.

The pre-neutron fragment mass distribution is one of the most important characteristics of the fission process. Nuclear modeling has made much progress in recent years, but a pure theoretical description of fragment mass distributions is far from being achieved.

Consequently the fragment mass and total kinetic-energy distributions currently used as input in the calculation of different quantities characterizing the fission process are experimental data.

At higher incident neutron energies a number of compound nuclei are undergoing fission (fission chances), each with its characteristic fission fragment distributions. Each of them will contribute to the experimentally measured fission observables.

New experiments regarding the fragment distributions of the neutron-induced fission of ^{238}U with energies up to 100 MeV were recently performed. The neutron source at the Los Alamos Neutron Science Center - Weapons Neutron Research (LANSCE-WNR), which provides neutrons from the intermediate to the fast region ($En = 100'$s of keV to 100's of MeV), and a twin Frisch-grid ionization chamber were used in this experiment. The double energy ($2E$) analysis procedure is employed to calculate pre- and post-neutron emission data of fragments. This work is still in progress.

The prompt neutron distributions $\nu(A)$ are needed to recover the pre-neutron fragment masses and distributions from the experimental post-neutron fragment data. In the case of ^{238}U(n,f) experimental $\nu(A)$ data are completely missing. The only way is to use $\nu(A)$ predicted by models. Consequently the model calculation of $\nu(A)$ becomes a very important request. The present paper answers to this need.

Preliminary results of the pre-neutron fragment data of ^{238}U(n,f) up to $En = 30$ MeV were reported in Ref. [1]. These preliminary results were obtained by using for the $\nu(A)$ distribution either the data determined by a scaling method [2] or the $\nu(A)$ prediction of the GEF code [3–5]. The processing of experimental data was performed for ^{238}U(n,f) only up to $En = 30$ MeV.

The $\nu(A)$ distributions used to obtain preliminary data of pre-neutron fragments [i.e., $\nu(A)$ of GEF [3] and those obtained by the scaling method] revealed significant differences in the resulting data of pre-neutron fragments [1].

*Corresponding author: anabellatudora@hotmail.com

In this context the present $\nu(A)$ results, predicted by a different model than the one previously used, is welcome and useful. This was the main motivation of the present paper.

On the other hand the behavior of $\nu(A)$, exhibiting a characteristic shape usually called "sawtooth," is one of the most interesting aspects of the prompt emission in fission. This behavior has been investigated since the 1950s [6]. However the measurements of $\nu(A)$ were mainly restricted to either spontaneous or thermal neutron-induced fission of the major actinides. At higher incident neutron energies the information is very scarce, almost inexistent. The $\nu(A)$ distributions have been measured only for the neutron-induced fission of ^{235}U at $En = 0.5$ MeV and 5.5 MeV [7] and of ^{237}Np at $En =$ 0.8 MeV and 5.5 MeV [8] or for proton-induced fission [9]. The only quantity measured in sufficient amount for at least the major actinides is the total average prompt neutron number $\langle\nu\rangle_{\rm tot}$ as a function of incident neutron energy.

The present paper focuses on the $\nu(A)$ calculation for the fission of ^{238}U induced by fast neutrons with energies ranging from 1 MeV to 80 MeV. The Point-by-Point (PbP) model of prompt emission (described in Ref. [10] and references therein) is used for the first time at incident neutron energies where multiple fission chances are involved.

The PbP model calculations, including $\nu(A)$, are performed for each compound nucleus undergoing fission involved at a given *En*. The total $\nu(A)$ at this *En* is obtained by averaging the individual $\nu(A)$ corresponding to the fissioning compound nuclei over their fission chance probabilities. At the upper limit of the present calculation, $En = 80$ MeV, the fission of ten nuclei of the main nucleus chain $^{239-230}$U and eight nuclei of the secondary nucleus chain $^{238-232}$Pa were taken into account. The fission chance probabilities are expressed by the total and partial fission cross-section ratios RF (for details, see Ref. [11] and references therein).

The $\nu(A)$ results of this paper will be used in the processing of measured post-neutron data. Taking into account that the preliminary results reported in Ref. [1] were based on the $\nu(A)$ predicted by the GEF code, a comparison between the $\nu(A)$ results of PbP and GEF is also included in this paper. It is expected that the differences in shape and magnitude between $\nu(A)$ of GEF and PbP are reflected in more or less significant differences in the pre-neutron fragment data.

In this sense in Ref. [12] an analysis of the sensitivity of the pre-neutron fragment mass distribution to the neutron evaporation correction has been performed. In this paper, $\nu(A)$ provided by the scaling method is used under two assumptions, i.e., the traditional one in which the excess neutrons are distributed equally across the mass distribution and another one in which the neutrons are predominantly emitted by the heavy fragments. The resulting difference in pre-neutron fragment mass yield amounted to 20%–30% for the most abundant fragments.

The aim of the present paper is the description of the developed model giving the $\nu(A)$ distribution at incident neutron energies where multiple fission chances are involved.

Taking into account that the present $\nu(A)$ results as well as those of other models or procedures used to recover the pre-neutron fragment data are predictions, the possibility of an indirect validation of these $\nu(A)$ results is welcome and recommended. A such indirect validation is proposed in the present paper.

The shape of $\nu(A)$ and its evolution with increasing *En* is important on one side for applications, i.e., the use of $\nu(A)$ in the process of recovering pre-neutron fragment data at high *En* and on the other hand for a better understanding of the prompt emission at high *En*. The evolution of the $\nu(A)$ shape with increasing *En* is explained by the influence of the shell effects of fragments. It is well known that the shell effects become less pronounced with increasing energy. The influence of shell effects is reflected in the fragment level-density parameters entering the partition of the excitation energy at scission. At high excitation energies of the fissioning nucleus the level-density parameter of a great part of the fragments tends to the asymptotic value. This fact leads to a smooth and almost linear increase in the fragment excitation energy with the fragment mass number and consequently to a smooth and almost linear behavior of $\nu(A)$.

II. BASIC FEATURES OF THE MODELING

At incident neutron energies up to about 25–30 MeV only the fission of nuclei of the main nucleus chain, formed by neutron emission from the precursor nucleus of this chain, has been considered. At *En* above 30 MeV charged particle emission occurs, and the fission of nuclei of secondary chains must be taken into account, too.

Prompt neutron and γ-ray emission from nuclei of the secondary chains was already included in the extended Los Alamos model (LAM) described in Refs. [10,11].

In Ref. [11] the extended LAM was applied to ^{238}U(n,f) at *En* up to 80 MeV by taking into account the following nucleus chains and ways.

(i) The main nucleus chain, indexed (1), with successive neutron evaporation from the precursor of this chain.
(ii) The proton way (labeled "p") consisting of proton emission from the nuclei of the main chain, leading to the formation of the secondary nucleus chain, indexed (2).
(iii) The way named "neutron via proton" (labeled "nvp") consisting of successive neutron evaporation from the precursor of the secondary chain (2).
(iv) The "deuteron" way consisting of deuteron emission from the nuclei of the main chain also leading to nuclei of the secondary chain (2).
(v) The "α" way consisting of α emission from the nuclei of the main chain, leading to the formation of another secondary nucleus chain, indexed (3).
(vi) The "neutron via α" way consisting of successive neutron evaporation from the precursor of the secondary chain (3).

The recursive formulas giving the average excitation energies of the fissioning nuclei formed by the six ways mentioned above can be found in Ref. [11].

The fission probabilities of each compound nucleus formed by the ways mentioned above are expressed by the so-called total and partial fission cross-section ratios (RF). In Ref. [11] and in the present paper the total and partial RF of the

Bruyères-le-Châtel (BRC) evaluation [13] were used. The plots of these total and partial RF reported in Ref. [11] clearly show that RF of the secondary Th chain (including the ways α and neutron via α) and the partial RF of the deuteron way are very low (of about 10^{-3} and less than 10^{-3}, respectively). Consequently, in this paper the contribution of the Th chain and of the deuteron way have been neglected.

PbP calculations were performed for the fissioning nuclei of the main Uranium chain and the secondary Protactinium chain formed by the ways proton (ii) and neutron via proton (iii) at average excitation energies given by the following recursive formulas:

$$\begin{aligned} Ex_1^{(1)} &= En + Bn_1^{(1)}, \\ \langle Ex\rangle_i^{(1)} &= \langle Ex\rangle_{i-1}^{(1)} - Bn_{i-1}^{(1)} - \langle \varepsilon_{ev}\rangle_{i-1}^{(1)}, \\ i &= 2,\ldots,N^{(1)}, \end{aligned} \tag{1}$$

in which "i" denotes the fission chance and $N^{(1)}$ is the number of nuclei of the main chain. $\langle Ex\rangle^{(1)}$ are the average excitation energies of the nuclei of the main chain, and $Bn^{(1)}$ are the neutron binding energies in these compound nuclei. $\langle \varepsilon_{ev}\rangle^{(1)}$ are the average energies in the center-of-mass system of the evaporated neutron before fission,

$$\langle Ex\rangle_i^{(p)} = \langle Ex\rangle_i^{(1)} - S_{pi}^{(1)} - \langle \varepsilon_{ev}\rangle_{pi}, \quad i = 1,\ldots,N^{(2)}, \tag{2}$$

$$\begin{aligned} \langle Ex\rangle_i^{(pn)} &= \langle Ex\rangle_{i-1}^{(pn)} - Sn_{i-1}^{(2)} - \langle \varepsilon_{ev}\rangle_{n,i-1}^{(2)}, \\ i &= 2,\ldots,N^{(2)}, \\ \langle Ex\rangle_1^{(pn)} &= \langle Ex\rangle_1^{(p)}. \end{aligned} \tag{3}$$

In Eqs. (2) and (3) $N^{(2)}$ is the number of nuclei of the secondary chain (2), $Sp^{(1)}$ are the proton separation energies from the nuclei of the main chain, $Sn^{(2)}$ are the neutron separation energies from the nuclei of the secondary chain, and $\langle \varepsilon_{ev}\rangle_p$ and $\langle \varepsilon_{ev}\rangle_n^{(2)}$ are the average energies of the evaporated proton and neutron before fission, respectively.

For all U and Pa fissioning nuclei, the fragmentation range taken in PbP model calculations is constructed as follows (for details, see Ref. [10] and references therein).

For each fragment mass number A covering a large range from symmetric fission up to a very asymmetric split (e.g., corresponding to a heavy fragment mass of about 160–165) three charge numbers Z are taken as the nearest integer values above and below the most probable charge Z_p taken as the unchanged charge distribution (UCD) corrected with the charge polarization ΔZ: $Z_p(A) = Z_{\rm UCD}(A) + \Delta Z(A)$. According to the sensibility studies reported in Ref. [14] the same value $\Delta Z = |0.5|$ is taken for all fragmentations (with a plus sign for light fragments and a minus sign for the complementary heavy ones). The isobaric charge distributions are taken as Gaussian functions centered on $Zp(A)$ with the same root-mean-square value of 0.6.

The features of the PbP model of prompt emission were already described in previous publications, see, for instance, Ref. [10] and references cited therein. Here we mention only that the compound nucleus cross sections of the inverse process of neutron evaporation from all nuclei forming the fragmentation ranges of the fissioning nuclei of the U and Pa chains are provided by optical model calculations with the computer code SCAT2 [15] using the phenomenological potential of Becchetti-Greenlees [16]. The level-density parameters of the fragments are calculated in the frame of the superfluid model of Ignatiuk [17] (with shell corrections of Möller and Nix [18] entering the superfluid formula) two times: First at scission by an iterative procedure providing simultaneously the level-density parameters and the excitation energies at scission (for details, see Refs. [10,19,20]). Second the level-density parameters are calculated at full acceleration, i.e., at the fragment excitation energies resulting from the partition of total excitation energy (TXE) by modeling at scission. The mass excesses entering the Q-values of the fragmentations and the neutron separation energies from fragments in the sequential emission are those of Audi and Wapstra taken from RIPL3 [21].

The PbP results of prompt neutron multiplicity of the fragments corresponding to each fissioning nucleus involved in the reaction $n + {}^{238}$U at a given En are averaged over the isobaric charge distributions, giving the individual prompt neutron multiplicity distribution $\nu_i(A)$.

The total $\nu(A)$ at a given En is then calculated by averaging these individual $\nu_i(A)$ over the fission chance probabilities (expressed by total and partial RF),

$$\nu(A) = \sum_{k=1}^{3}\sum_{i=1}^{N(k)} {\rm RF}_i^{(k)}\nu_i^{(k)}(A), \tag{4}$$

in which k denotes the three ways (i)–(iii) taken into account and the index i is running over the nuclei of each chain or way.

The prompt neutron multiplicity of a fragment pair $\nu(A,Z) = \nu(A_L,Z_L) + \nu(A_H,Z_H)$ averaged over the isobaric charge distribution gives the individual $\nu_{{\rm pair}\,i}(A)$. This quantity showed a very weak dependence on the TXE partition, for details see Ref. [14]. Moreover, except for the near-symmetric fragmentations (i.e., pairs with $A_H < 130$), the individual $\nu_{{\rm pair}\,i}(A)$ exhibits a weak variation with A (see, e.g., Fig. 5).

The total average multiplicity of fragment pairs is also obtained by averaging the individual $\nu_{{\rm pair}\,i}(A)$ over the fission chance probabilities,

$$\nu_{\rm pair}(A) = \sum_{k=1}^{3}\sum_{i=1}^{N(k)} {\rm RF}_i^{(k)}\nu_{{\rm pair}\,i}^{(k)}(A). \tag{5}$$

Because of its weak dependence on the TXE partition and the weak variation with the mass number A in the asymmetric fission region, the total $\nu_{\rm pair}(A)$ of Eq. (5) is useful for indirect validations, i.e., its level of magnitude can be compared with the total average multiplicity of prompt neutrons emitted by fragments $\langle\nu\rangle_{\rm FF}$.

The total average number of prompt neutrons emitted by the fission fragments (FF) can be obtained by averaging the prompt neutron distribution $\nu(A)$ of Eq. (4) [or $\nu_{\rm pair}(A)$ of Eq. (5)] over a fragment mass distribution $Y(A)$,

$$\langle\nu\rangle_{\rm FF} = \sum_A \nu(A)Y(A)/\sum_A Y(A). \tag{6}$$

At incident neutron energies where only one fission chance is involved $\langle\nu\rangle_{\rm FF}$ is just the total average number of prompt

neutrons $\langle\nu\rangle_{\rm tot}$ which is experimentally measured. At higher *En* where multiple fission chances are involved, this total average number of prompt neutrons is the sum of $\langle\nu\rangle_{\rm FF}$ emitted by fission fragments and the total average number of neutrons evaporated from the compound nuclei before fission, usually named pre-fission neutrons $\langle\nu\rangle_{\rm prefiss}$,

$$\langle\nu\rangle_{\rm tot} = \langle\nu\rangle_{\rm FF} + \langle\nu\rangle_{\rm prefiss}. \quad (7)$$

The average number of pre-fission neutrons depends on the probability of nuclei formed by neutron evaporation from the precursor of the main chain, way (i), and from the secondary chains by way (iii) (neutron via proton) and way (vi) (neutron via α). It can be calculated as

$$\langle\nu\rangle_{\rm prefiss} = \sum_{k=1,3,6}\sum_{i=1}^{N(k)}(i-1){\rm RF}_i^{(k)}, \quad (8)$$

in which $k = 1$, 3, and 6 denotes the ways (i), (iii), and (vi) and ${\rm RF}^{(1)}$ is the total RF of the U chain. ${\rm RF}^{(3)}$ and ${\rm RF}^{(6)}$ are the partial fission cross-section ratios of the ways neutron via proton and neutron via α calculated on the basis of production cross sections as described in Ref. [11].

As it was already mentioned in the Introduction, experimental $\nu(A)$ data are very scarce. They are completely missing for many fissioning systems including $^{238}{\rm U}(n,f)$. Consequently a direct validation of calculated $\nu(A)$ by comparison with experimental data is very limited. The only quantity measured in sufficient amount is $\langle\nu\rangle_{\rm tot}$ as a function of *En*.

In the case of $^{238}{\rm U}(n,f)$ such experimental data can be found in the EXFOR library [22], e.g., many data sets covering the energy range below the second fission chance threshold, the data sets of Fréhaut going up to *En* of about 15 and 28 MeV, respectively, the data of Taieb *et al.* [23] and Ethvignot *et al.* [24] measured up to $En = 200$ MeV, and a recent data set covering the *En* range from 1.4 to 19.1 MeV [25].

These data can serve for an indirect validation of $\nu(A)$ results, especially in the *En* range where only the first fission chance is involved due to the existence of reliable experimental $Y(A)$ data allowing to apply Eq. (6). As it will be demonstrated in the next sections, the $\langle\nu\rangle_{\rm tot}$ value is strongly influenced by the $\nu(A)$ distribution, whereas the $Y(A)$ distribution has only a weak influence. This fact justifies the comparison of $\langle\nu\rangle_{\rm tot}$ with experimental data as an indirect validation of $\nu(A)$.

III. POINT-BY-POINT MODEL CALCULATIONS OF $\nu(A)$

A. PbP results of $\nu(A)$ at incident neutron energies below the second fission chance threshold

PbP calculations for $^{238}{\rm U}(n,f)$ at *En* up to 5 MeV were already performed. In Ref. [26], focusing on the effects of sub-barrier fission on fragment properties, a part of these PbP results (referring to $\langle\nu\rangle_{\rm tot}$ and prompt neutron spectrum) were reported. They were obtained by averaging the corresponding multiparametric matrices (as primary PbP results) over the fragment distributions based on the experimental data measured at Joint Research Center-Institute for Reference Materials and Measurements (JRC-IRMM) in two campaigns (at *En* ranging from 0.9 to 2 MeV [27] and at *En* above 2 MeV up to 5.8 MeV [28]).

Examples of PbP results of $\nu(A)$ at six incident neutron energies ranging from 1 to 5 MeV are plotted with black stars in Fig. 1.

Note, the increase of $\nu(A)$ with increasing *En* for heavy fragments only, observed experimentally in the cases of $^{235}{\rm U}(n,f)$ [7] and $^{237}{\rm Np}(n,f)$ [8] were well reproduced by the PbP results (e.g., reported in Refs. [10,19,20]. It was also confirmed by other PbP results of $\nu(A)$, e.g., for $^{232}{\rm Th}(n,f)$ [29] and $^{234}{\rm U}(n,f)$ [30]. This behavior of $\nu(A)$ is visible in the present case too. See Fig. 2 where the $\nu(A)$ results given with black stars in Fig. 1 are plotted together.

1. Comparison with $\nu(A)$ of the GEF code

The PbP results of $\nu(A)$ for $^{238}{\rm U}(n,f)$ in the *En* range below the second fission chance threshold were compared with those provided by the last two versions of the GEF code, i.e., the version 2014/2.1 [3] (denoted in the following as GEF-2014) and the last version 2015/2.2 released in Sept. 2015 with subsequent corrections [4] (denoted in the following as GEF-2015).

Note, as it was already mentioned in the Introduction, the comparison of present $\nu(A)$ prediction with the one of GEF is justified by the use of $\nu(A)$ results of GEF-2014 in the processing of post-neutron data leading to the preliminary pre-neutron fragment distributions reported in Ref. [1].

In Fig. 1 the $\nu(A)$ results of GEF-2014 are plotted with open blue squares, and those of GEF-2015 are plotted with full red circles. Results of the scaling method, also used in Ref. [1], are exemplified at $En = 3$ MeV and 5 MeV (continuous dark yellow lines).

As it can be seen $\nu(A)$ of PbP and GEF-2014 are in overall reasonable agreement in the asymmetric fission region. It is interesting to see that $\nu(A)$ of both GEF versions exhibit a plateau at A between 140 and 150. In this A region the $\nu(A)$ results of GEF-2015 at *En* above 2 MeV are visibly higher than both $\nu(A)$ of GEF-2014 and PbP. Differences between the $\nu(A)$ results of both GEF versions and PbP are visible near symmetric fission too.

The results of the scaling method differ significantly from the ones of PbP and GEF.

2. Indirect validation of $\nu(A)$ results

Total average prompt neutron multiplicities $\langle\nu\rangle_{\rm tot}$ obtained by averaging $\nu(A)$ of PbP and GEF over two $Y(A)$ distributions are compared. The $Y(A)$ distributions are those provided by the GEF code, plotted with red circles in Fig. 3 and the experimental data of JRC-IRMM [27,28] given in this figure with different black and gray symbols. Visible differences between $Y(A)$ of GEF and experimental data exist. The $Y(A)$ results of GEF exhibit a visible staggering at the top of the distribution. This staggering is very pronounced at lower *En*. Hence the differences between $Y(A)$ of GEF and JRC-IRMM are therefore larger at lower *En*.

The $\nu(A)$ results of PbP and GEF-2015 are averaged over these $Y(A)$ distributions as follows, see Fig. 4:

(a) The $\nu(A)$ of PbP is averaged over the experimental $Y(A)$ data of JRC-IRMM (red circles) and the $Y(A)$ of GEF-2015 (orange up-triangles).

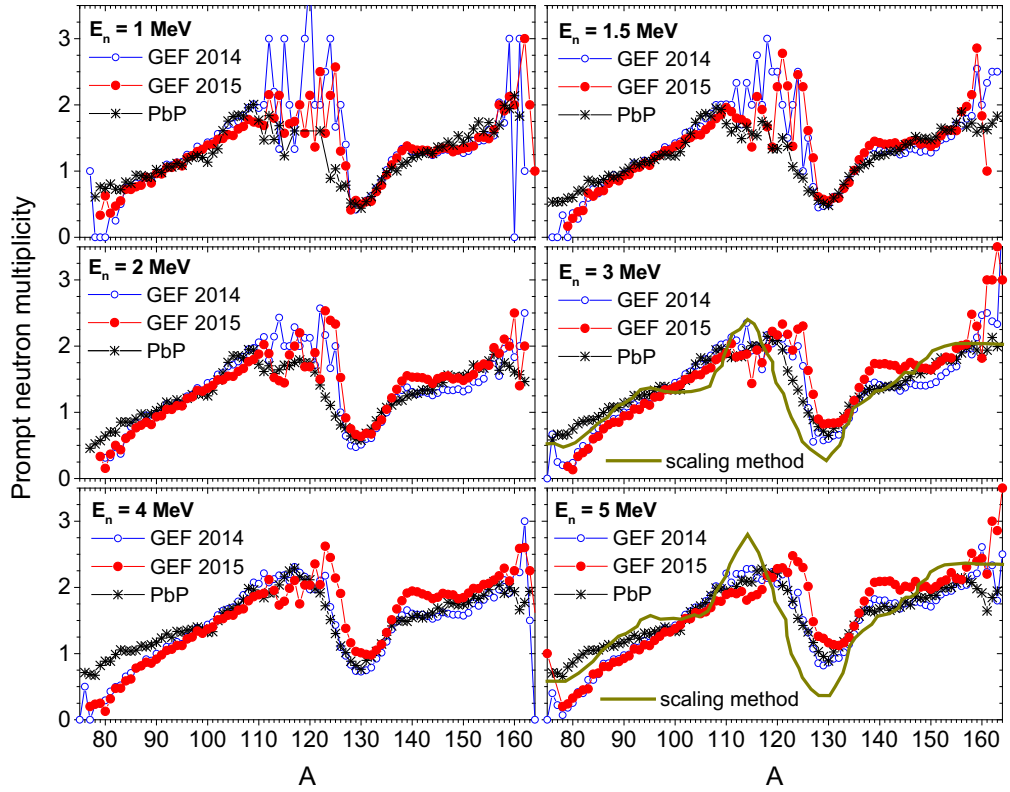

FIG. 1. $\nu(A)$ results of PbP (black stars) in comparison with the $\nu(A)$ results of GEF-2014 (open blue circles) and GEF-2015 (red circles) at incident energies where only the first fission chance is involved. Examples of $\nu(A)$ given by the scaling method, used to obtain the preliminary recovered pre-neutron fragment distributions reported in Ref. [1], are given with continuous dark-yellow lines.

(b) The $\nu(A)$ of GEF-2015 is averaged over $Y(A)$ of GEF-2015 (blue diamonds) and $Y(A)$ of JRC-IRMM (green down-triangles).

Note, the $\langle\nu\rangle_{\rm tot}$ result plotted with red circles was already reported in Ref. [26]. $\langle\nu\rangle_{\rm tot}$ plotted with blue diamonds is the output of GEF-2015. The differences between these $\langle\nu\rangle_{\rm tot}$ results do not exceed 4%.

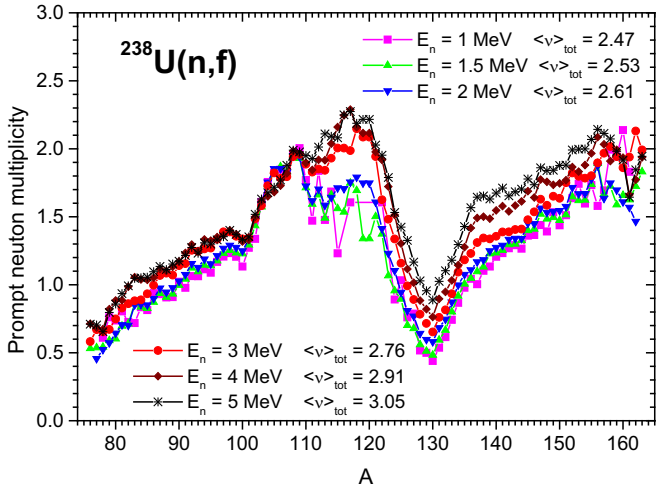

FIG. 2. PbP results of $\nu(A)$ at *En* ranging from 1 to 5 MeV. The corresponding $\langle\nu\rangle_{\rm tot}$ values obtained by averaging $\nu(A)$ over the experimental $Y(A)$ data of JRC-IRMM are indicated in the figure too.

From Fig. 4 it is clear that

(a) The $\nu(A)$ of PbP averaged over the $Y(A)$ distributions of JRC-IRMM and GEF-2015 gives very close results (red circles compared with orange up-triangles)

(b) The $\nu(A)$ of GEF averaged over $Y(A)$ of JRC-IRMM and GEF-2015 gives very close results, too (green down-triangles compared with blue diamonds).

Taking into account the visible differences between the $Y(A)$ distributions of JRC-IRMM and GEF (illustrated in Fig. 3) this exercise demonstrates that a much stronger influence in $\langle\nu\rangle_{\rm tot}$ is played by the $\nu(A)$ distribution compared to the $Y(A)$ distribution. Consequently the differences between the values of $\langle\nu\rangle_{\rm tot}$ resulting from the use of the $\nu(A)$ distributions of GEF and PbP (visible in Fig. 4) are mainly due to the differences between these distributions.

The fact that the $\langle\nu\rangle_{\rm tot}$ value is strongly dependent on the $\nu(A)$ distribution, whereas the $Y(A)$ distribution has only a weak influence as demonstrated by this exercise, justifies the comparison of $\langle\nu\rangle_{\rm tot}$ with experimental data as an indirect validation of the $\nu(A)$ results.

As it can be seen in Fig. 4 the $\langle\nu\rangle_{\rm tot}$ results of GEF-2015 (blue and green symbols) overestimate the majority of experimental data (being in agreement only with data of Taieb *et al.* [23]) whereas the PbP results (red and orange symbols) are much closer to the experimental data.

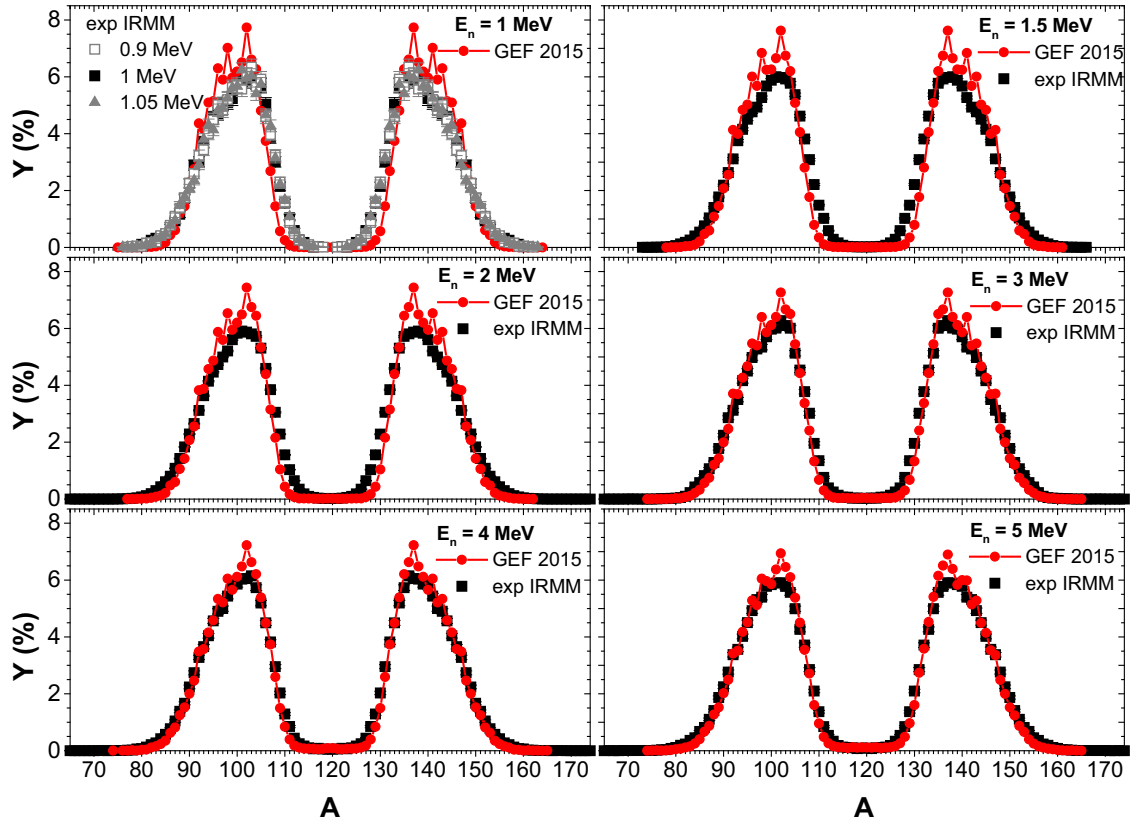

FIG. 3. Comparison of the $Y(A)$ distributions of GEF-2015 (red circles) with the experimental data of JRC-IRMM (black and gray symbols) at En where only the first fission chance is involved.

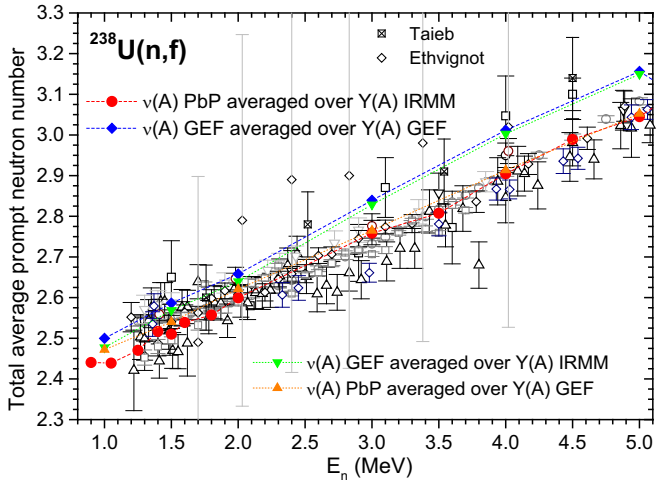

FIG. 4. $\langle\nu\rangle_{\rm tot}$ in the En range where only the first fission chance is involved: experimental data (different open symbols) and results obtained by averaging the prompt neutron distribution $\nu(A)$ of PbP and GEF-2015 over the experimental $Y(A)$ data of JRC-IRMM and the $Y(A)$ results of GEF-2015 as follows: $\nu(A)$ of PbP averaged over $Y(A)$ of JRC-IRMM with red circles; $\nu(A)$ of GEF-2015 averaged over $Y(A)$ of GEF-2015 with blue diamonds; $\nu(A)$ of PbP averaged over $Y(A)$ of GEF-2015 with orange up-triangles; $\nu(A)$ of GEF-2015 averaged over $Y(A)$ of JRC-IRMM with green down-triangles.

B. PbP calculation of $\nu(A)$ at incident neutron energies where multiple fission chances are involved

The PbP calculations were performed at incident neutron energies ranging from 6 MeV to 80 MeV. For each fissioning nucleus involved in the reaction at a given En, these calculations are performed at the average excitation energies given by Eq. (1) for U nuclei, Eq. (2) for Pa nuclei formed by proton emission from the U chain, and Eq. (3) for Pa nuclei formed by neutron emission from the precursor of the same chain (the neutron via proton way).

Examples of individual $\nu(A)$ and $\nu_{\rm pair}(A)$ (corresponding to each fissioning nucleus) are given in Fig. 5 with open symbols for the nuclei of the main U chain and solid lines for the nuclei of the secondary Pa chain (including both contributions of the proton and neutron via proton ways). The total average $\nu(A)$ and $\nu_{\rm pair}(A)$ obtained by averaging the individual prompt neutron multiplicities over the fission chance probabilities according to Eqs. (4) and (5) are plotted with full black circles. Note, at $En = 6$ and 10 MeV the RF values are also given in the legend. The total $\nu_{\rm pair}(A)$ resulting from the systematic of Wahl [31] are exemplified with gray stars. It can be seen that our results of total $\nu_{\rm pair}(A)$ are very close to the systematic of Wahl [31] in the asymmetric fission region. More details regarding the comparison of PbP and GEF results with the Wahl [31] systematic are given in Sec. III B 2.

As it can be seen in the lower part of Fig. 5 ($En =$ 50 MeV and 80 MeV) the sawtooth shapes of individual $\nu(A)$

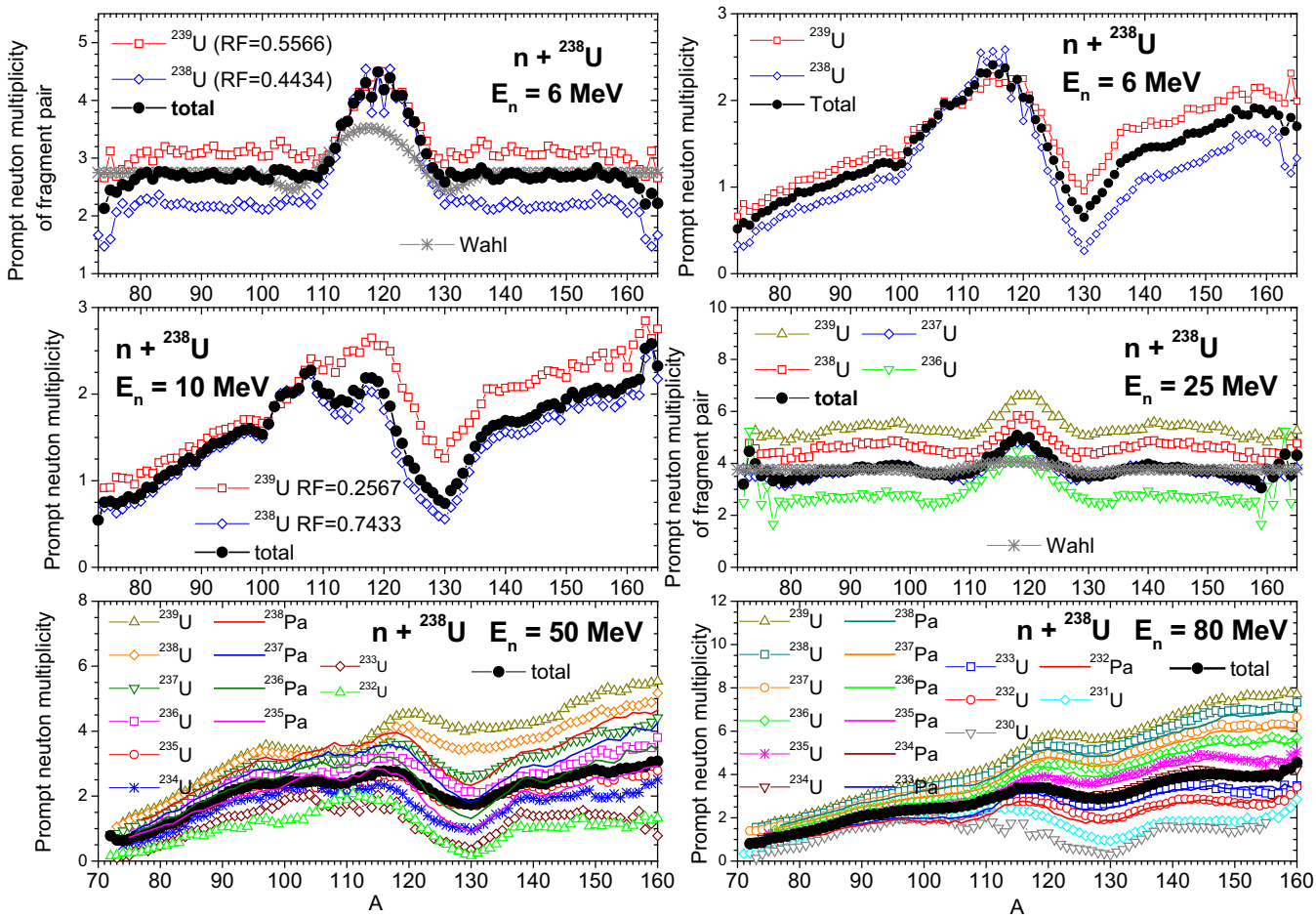

FIG. 5. Examples of $\nu(A)$ and $\nu_{\text{pair}}(A)$ results at incident neutron energies where multiple fission chances are involved. The individual $\nu(A)$ and $\nu_{\text{pair}}(A)$ are plotted with open symbols for U nuclei and solid lines for Pa nuclei. The total $\nu(A)$ and $\nu_{\text{pair}}(A)$ are plotted with full black squares. Examples of $\nu_{\text{pair}}(A)$ of the Wahl systematic [31] are given with gray stars.

corresponding to the first few compound nuclei of the U and Pa chains (having the highest excitation energies) has almost vanished. The explanation is the damping of shell effects of a great part of the fragments coming from these compound nuclei. In other words the excitation energies of many fully accelerated fragments are high enough to reach the asymptotic values of their level-density parameters (a detailed discussion about it is given in Sec. III C).

Examples of total $\nu(A)$ calculated at ten incident energies ranging from 6 to 80 MeV are plotted together in Fig. 6. A less pronounced sawtooth shapes of total $\nu(A)$ with increasing *En* is clearly visible.

It is well established and confirmed by experimental $\nu(A)$ data that, with increasing *En,* the excess of excitation energy goes mainly to the heavy fragments, leading to an increase in $\nu(A)$ mainly for heavy fragments.

The shapes of the total $\nu(A)$ plotted in Fig. 6 are resulting from a combination of the shapes of individual $\nu(A)$ (with a more or less pronounced sawtooth character depending on the amount of excitation energy of the respective fissioning nucleus) and the magnitude of their probabilities (expressed by RF). This fact can lead to different slopes of the left wings of the total $\nu(A)$ at different *En.*

The total $\nu(A)$ distribution [given by Eq. (4)] depends on the probabilities of fission chances (expressed as fission cross-section ratios). As was mentioned in Sec. II, the results

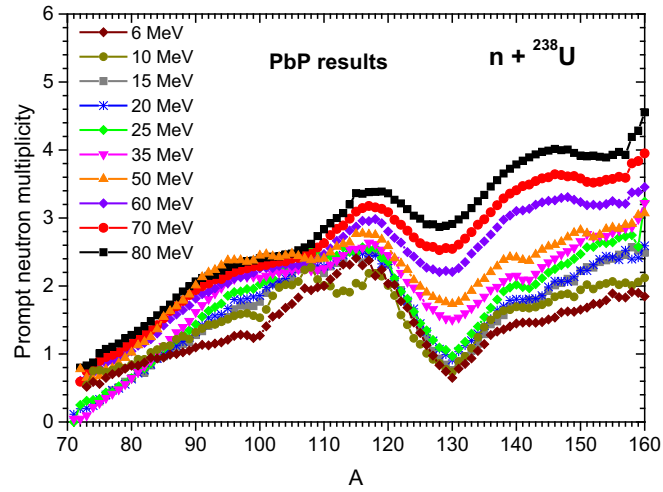

FIG. 6. PbP results of total $\nu(A)$ at incident neutron energies were multiple fission chances are involved.

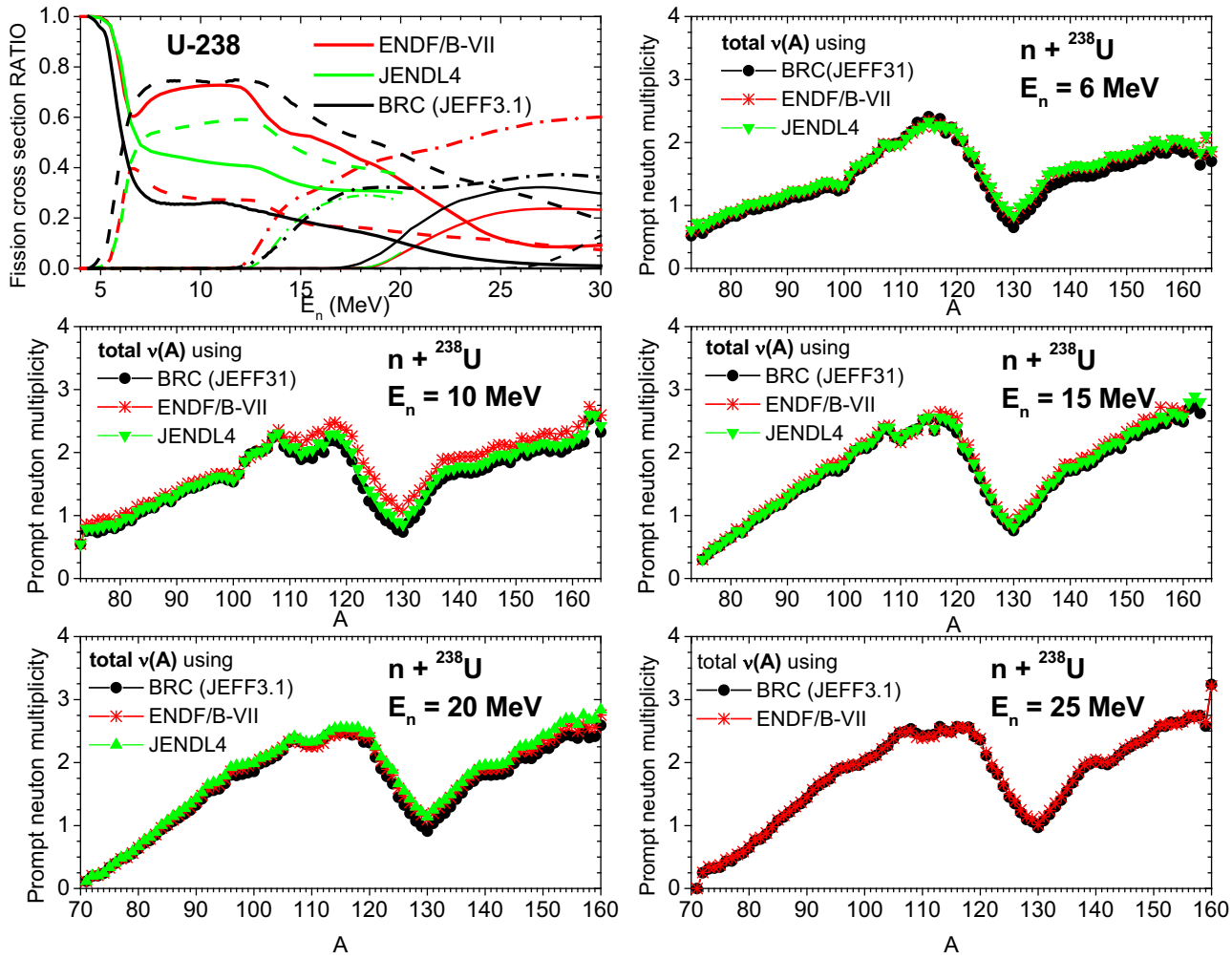

FIG. 7. Left upper part: fission cross-section ratios of the ENDF/B-VII (red lines), JENDL4 (green lines), and BRC (black lines) evaluations. RF of the first fission chance are plotted with thick solid lines, RF of the second chance are plotted with dashed lines, RF of the third chance are plotted with dashed-dotted lines, RF of the fourth chance are plotted with this solid lines, and RF of the 5th chance are plotted with thin dashed lines. Others: examples of total $\nu(A)$ obtained by averaging the PbP results of individual $\nu(A)$ over RF of ENDF/B-VII (red stars), JENDL4 (green triangles), and BRC (black circles).

given in Figs. 5 and 6 were obtained with RF of the BRC evaluation. Taking into account the important role played by the shape and the magnitude of the $\nu(A)$ in the recovering of pre-neutron fragment data in a $2E$ analysis procedure, it is interesting to see if the differences between $\nu(A)$ obtained with RF of different evaluations are significant or not. In the case of the ENDF/B-VII evaluation [32] the upper limit of the incident neutron energy is 30 MeV, and for JENDL4 [33] it is 20 MeV. Consequently in this comparison only the contribution of the individual $\nu(A)$ of fissioning nuclei of the main U chain is involved.

The RF resulting from the fission cross sections of ENDF/B-VII (red lines) and JENDL4 (green lines) are plotted in the upper left panel of Fig. 7 together with RF of the BRC/JEFF3.2 evaluation [13] (black lines). Differences between RF of these evaluations are clearly visible.

The total $\nu(A)$ at five En ranging from 6 to 25 MeV, taken as examples, obtained by averaging the individual $\nu(A)$ resulting from PbP calculations over the RF of ENDF/B-VII and JENDL4 are plotted in Fig. 7 with red stars and green triangles, respectively. For comparison the total $\nu(A)$ obtained with RF of BRC are also given with black circles.

As can be seen the differences between the total $\nu(A)$ results obtained with different RF are almost insignificant. An exception is at $En = 10$ MeV where differences between $\nu(A)$ obtained with the RF of ENDF/B-VII and the ones based on RF of BRC and JENDL4 are distinguished in the heavy fragment region. These differences are due to the very different RF values of ENDF/B-VII and BRC at $En = 10$ MeV, i.e., RF of the first chance of ENDF (of about 0.72) is close to the RF value of the second chance of BRC and vice versa, and the RF of the second chance of ENDF (of about 0.28) is close to RF of the first chance of BRC.

1. Comparison with ν(A) of the GEF code

The comparison between $\nu(A)$ of PbP and GEF at En where multiple fission chances are involved is interesting for two reasons:

(a) The practical purpose, both $\nu(A)$ predictions can be used in the recovering of pre-neutron fragment data from the post-neutron fragment data recently measured at LANSCE.
(b) The assumptions and physical considerations on which the modeling of GEF is based differ from the ones of PbP and other prompt emission codes discussed in Ref. [10]. Moreover it is well established that the TXE partition is best reflected in the shape of the $\nu(A)$ distribution [as well as in the prompt γ-ray energy distributions $E\gamma(A)$].

A comparison between the $\nu(A)$ results of GEF-2015 (full red circles), GEF-2014 (open blue circles), and PbP (black stars) at ten incident neutron energies ranging from 6 to 80 MeV is given in Fig. 8. Results of the scaling method are also exemplified at $En = 15$ MeV and 20 MeV (continuous dark yellow lines).

As a general observation, it can be seen that at all *En* illustrated in this figure the $\nu(A)$ of both versions of GEF are higher than the $\nu(A)$ of PbP. Differences in shape between the $\nu(A)$ results of the versions of GEF are also visible at all *En* except at 6 MeV where the $\nu(A)$ of both versions of GEF are close to each other and close to the $\nu(A)$ of PbP too. The $\nu(A)$ results of the GEF versions differ especially in the mass range from 120 up to about 135–140. At high *En,* i.e., 70, 80 MeV, the $\nu(A)$ result of PbP has a visible tendency to a linear increase, exhibiting only a slight oscillation in the A region of symmetric fission compared to the line plotted in wine color. The $\nu(A)$ results of both GEF versions show more pronounced deviations from linearity.

It can be seen that $\nu(A)$ of the scaling method differ very much from the GEF and PbP results, exhibiting much more pronounced sawtooth shapes.

The differences between the $\nu(A)$ results of PbP and GEF can be understood by the principle differences between the TXE partition methods of PbP and GEF. These methods were analyzed in detail in Ref. [20]. Here we mention only that in the method of GEF the partition takes place before scission, the intrinsic energy being partitioned according to the "energy sorting mechanism" proposed by the authors of GEF. This sorting mechanism (parametrized in the GEF code) is supported by the following assumptions (Ref. [5] and references therein):

(a) The low values of the intrinsic energy in the case of thermal neutron-induced fission and spontaneous fission justifying the consideration of the fragment level densities in the constant temperature regime only.
(b) The neglection of the shell effects of the fragments, i.e. the parameter T of the constant temperature function of the level density is taken as $T \propto 1/A^{2/3}$.

In the GEF code the excitation energy at full acceleration is the sum of the following components: the intrinsic energy before scission (shared by the sorting mechanism), the collective energy (shared equally between the complementary fragments), the absolute deformation energy of fragments at scission, and the rotation energy of the fragments. The absolute deformation energy at scission has the largest contribution. It is based on a parametrization of the β_2 parameter at scission included in the GEF code, and this energy component practically drives the shape and the magnitude of the fragment excitation energy at full acceleration and consequently of $\nu(A)$.

In the TXE partition of PbP (described in detail in Refs. [20,19,10]) the partition takes place at scission, i.e., the excitation energy at scission is shared between the complementary fragments under the following assumptions:

(a) The amount of the excitation energy at scission is always sufficiently high, justifying the consideration of the fragment level densities in the Fermi-gas regime.
(b) The statistical equilibrium at scission, i.e., equal nuclear temperatures of complementary fragments.

Note, the prompt emission modeling of the probabilistic Monte Carlo codes intercompared in Ref. [10] are based on these assumptions, too.

The other energy component in the TXE partition of PbP is the extra-deformation energy of fragments, i.e., the difference between the absolute deformation energy of a fragment at scission and at full acceleration. This component is much smaller than the fragment excitation energy at scission.

In other words in the PbP model the shape and the magnitude of the fragment excitation energy at full acceleration and consequently of the $\nu(A)$ distribution is driven by the shape and the magnitude of the fragment excitation energy at scission resulting from the energy partition at scission. In this energy partition the shell effects of the fragments (entering the superfluid formula of the level-density parameters) play a very important role. The vanishing of the shell effects at high excitation energies of the fragments leads to the vanishing of the sawtooth shapes of individual $\nu(A)$ corresponding to the first few fissioning nuclei (open symbols in the lower part of Fig. 5), and the total $\nu(A)$ (black stars in the lower part of Fig. 8) exhibit only a still visible oscillation in the A region of symmetric fission compared to the line plotted in wine color in Fig. 8.

2. *Comparison of $\langle\nu\rangle_{\rm tot}$ results with experimental data and indirect validation of $\nu(A)$*

The total number of prompt neutrons $\langle\nu\rangle_{\rm tot}$ (full circles) and its components, the average number of pre-fission neutrons $\langle\nu\rangle_{\rm prefiss}$ (open circles), and the average number of neutrons emitted by fragments $\langle\nu\rangle_{\rm FF}$ (stars) are given in Fig. 9. The results of GEF-2015 are plotted in green color, and those of GEF-2014 are plotted in the blue color. Our results reported in Ref. [11] based on the extended LAM (considering only the most probable fragmentation with average values of model parameters based on the PbP treatment) are plotted in red color. Note, the average values of the LAM parameters corresponding to multiple compound nuclei undergoing fission were based on the PbP treatment too.

As it can be seen the $\langle\nu\rangle_{\rm prefiss}$ results of GEF-2014 and GEF-2015 are identical. They are lower than our $\langle\nu\rangle_{\rm prefiss}$ result [Eq. (8) with RF of the BRC evaluation]. The $\langle\nu\rangle_{\rm FF}$ result of GEF-2015 is higher than the result of GEF-2014 by

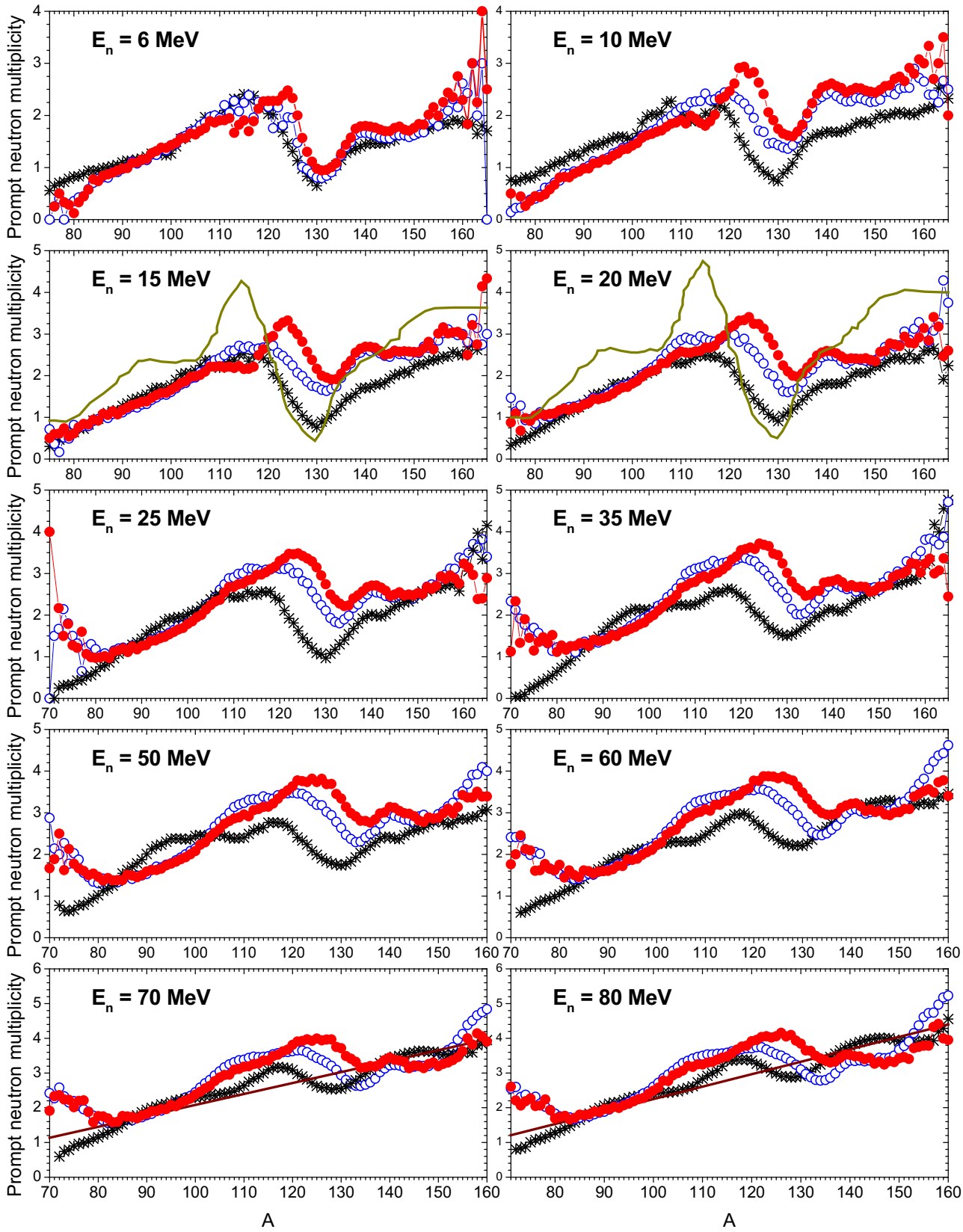

FIG. 8. Comparison of $\nu(A)$ results of PbP (black stars) with those of GEF-2015 (full red circles) and GEF-2014 (open blue circles) at ten incident neutron energies ranging from 6 MeV to 80 MeV. Results of the scaling method are exemplified with a continuous dark-yellow line at $En = 15$ MeV and 20 MeV.

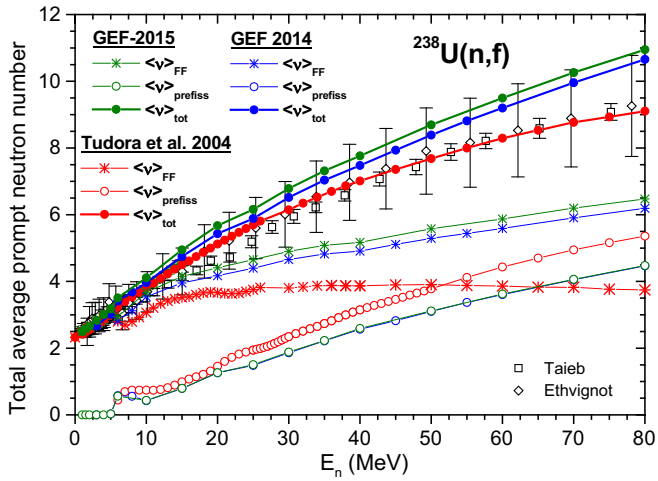

FIG. 9. Total average prompt neutron multiplicity $\langle\nu\rangle_{\rm tot}$ (full circles) as a sum of the average number of pre-fission neutrons $\langle\nu\rangle_{\rm prefiss}$ (open circles) and the average number of neutrons emitted by fragments $\langle\nu\rangle_{\rm FF}$ (stars) in comparison with experimental data (open black symbols). The results of the GEF version of 2014 are plotted in blue, and those of the GEF version of 2015 are plotted in green. Our results are plotted in red.

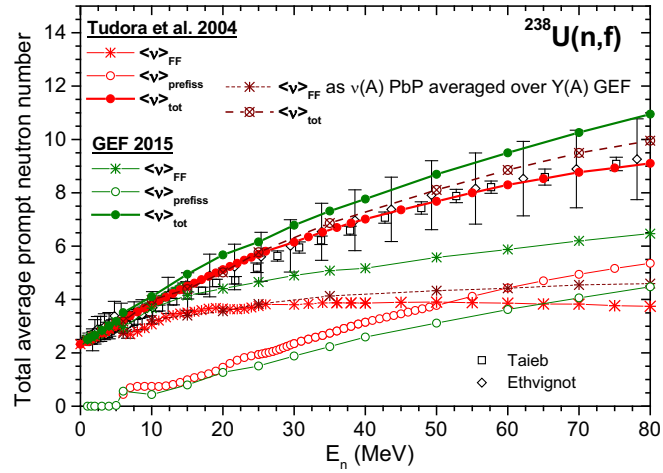

FIG. 10. $\langle\nu\rangle_{\rm tot}$ (full circles), $\langle\nu\rangle_{\rm FF}$ (stars), and $\langle\nu\rangle_{\rm prefiss}$ (open circles) of GEF-2015 (olive) and those reported in Tudora *et al.* [11] (red). $\langle\nu\rangle_{\rm FF}$ obtained by averaging $\nu(A)$ of PbP over $Y(A)$ of GEF are plotted with wine stars. The corresponding $\langle\nu\rangle_{\rm tot}$ (as a sum of this $\langle\nu\rangle_{\rm FF}$ and $\langle\nu\rangle_{\rm prefiss}$ of BRC) are plotted with wine circles with a cross inside.

$\sim$0.5 neutrons. Consequently the $\langle\nu\rangle_{\rm tot}$ result of GEF-2015 is also higher by $\sim$0.5 neutrons compared to the result of GEF-2014. Our $\langle\nu\rangle_{\rm FF}$ result from Ref. [11] (red stars) is much lower than the GEF results, and it is nearly constant (of about four neutrons) at *En* above 30 MeV. Both $\langle\nu\rangle_{\rm tot}$ results of GEF overestimate the experimental data of Taieb *et al.* [23] (open black squares) and remain inside the large error bars of the Ethvignot *et al.* [24] data (open black diamonds). Our $\langle\nu\rangle_{\rm tot}$ result of 2004 describes well the experimental data of Taieb *et al.* [23] and Ethvignot *et al.* [24].

Even though experimental $Y(A)$ distributions do not exist at *En* above 6 MeV, a comparison of $\langle\nu\rangle_{\rm tot}$ with experimental data remains possible by using the $Y(A)$ distributions provided by the GEF code. Consequently $\langle\nu\rangle_{\rm tot}$ is taken as a sum of $\langle\nu\rangle_{\rm prefiss}$ based on the RF of BRC (open red circles in Fig. 9) and $\langle\nu\rangle_{\rm FF}$ obtained by averaging the $\nu(A)$ of PbP over the $Y(A)$ of GEF-2015. This comparison is illustrated in Fig. 10 ($\langle\nu\rangle_{\rm FF}$ with wine stars and $\langle\nu\rangle_{\rm tot}$ with wine circles with a cross inside).

As it can be seen this $\langle\nu\rangle_{\rm FF}$ is very close to our result of Ref. [11] up to about 50 MeV, and it is higher by about 0.5 neutrons above this energy. The resulting $\langle\nu\rangle_{\rm tot}$ is in very good agreement with the experimental data up to about 50 MeV. Above this energy it is higher than the data but still lower compared to the $\langle\nu\rangle_{\rm tot}$ of GEF, which overestimates the data more.

As a simple observation, the higher $\nu(A)$ distributions of GEF compared to those of PbP, see Fig. 8, are reflected in the much higher $\langle\nu\rangle_{\rm FF}$ and $\langle\nu\rangle_{\rm tot}$ results of both GEF versions compared to those of PbP.

The deviation of PbP and GEF results from the systematic of Wahl [31] can be estimated by comparing $\langle\nu\rangle_{\rm FF}$ obtained by averaging the $\nu(A)$ distributions of Wahl [31], PbP, and GEF over the same $Y(A)$ distributions as follows.

The multiplicity distributions of Wahl, PbP and GEF at $En = 6$ MeV and 25 MeV (plotted in Fig. 5) are taken as example. At $En = 6$ MeV two $Y(A)$ distributions can be used, the experimental data of JRC-IRMM [28] plotted in Fig. 11 with full black squares and the $Y(A)$ result of GEF-2015 given with full red circles. At $En = 25$ MeV the $\nu(A)$ distributions of Wahl, PbP and GEF were averaged only over the $Y(A)$ distribution of GEF-2015 plotted with open green circles in Fig. 11.

The obtained $\langle\nu\rangle_{\rm FF}$ are given in Table I together with the deviations of the $\langle\nu\rangle_{\rm FF}$ results of GEF and PbP from the ones

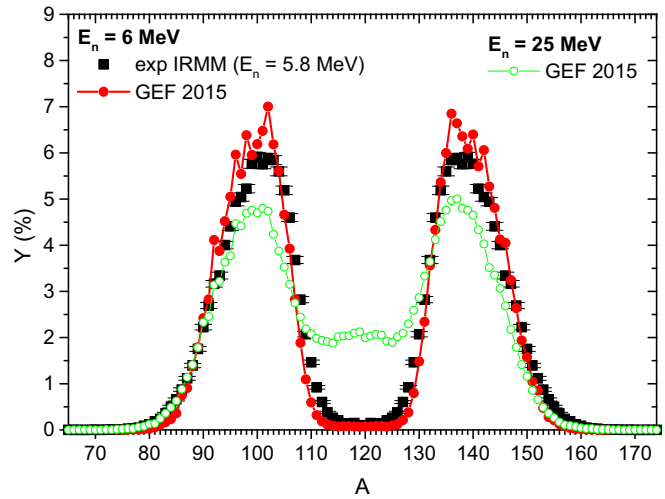

FIG. 11. $Y(A)$ distributions used to compare $\langle\nu\rangle_{\rm FF}$ based on $\nu(A)$ distributions of PbP, Wahl, and GEF: $Y(A)$ of GEF at $En = 6$ MeV with red circles, experimental $Y(A)$ data of JRC-IRMM at $En = 5.8$ MeV with black squares, and $Y(A)$ of GEF at $En = 25$ MeV with open green circles.

TABLE I. $\langle\nu\rangle_{\rm FF}$ obtained by averaging the $\nu(A)$ of Wahl, PbP, and GEF over a given $Y(A)$ and the deviation of the PbP and GEF results from Wahl.

$\nu(A)$	$Y(A)$	$\langle\nu\rangle_{\rm FF}$	Deviation from Wahl [31]
	$En = 6$ MeV		
Wahl [31]	Expt. JRC-IRMM (5.8 MeV)	2.6912	
PbP	Expt. JRC-IRMM (5.8 MeV)	2.7679	2.85%
GEF-2015	Expt. JRC-IRMM (5.8 MeV)	2.9715	10.42%
Wahl [31]	GEF	2.6874	
PbP	GEF	2.7336	1.72%
GEF-2015	GEF	2.9466	9.65%
	$En = 25$ MeV		
Wahl [31]	GEF	3.7720	
PbP	GEF	3.8313	1.57%
GEF-2015	GEF	4.6527	23.35%

of Wahl. As it can be seen the $\langle\nu\rangle_{\rm FF}$ of PbP and Wahl are close to each other (differences less than 3%) whereas the $\langle\nu\rangle_{\rm FF}$ of GEF-2015 differ significantly from those of Wahl (∼10% at 6 MeV and 23% at 25 MeV).

Consequently we believe that the visible differences in shape and magnitude between the $\nu(A)$ results of PbP and GEF at En where multiple fission chances are involved will lead to non-negligible differences between the pre-neutron fragment data based on these predictions.

C. Disappearing sawtooth characters of individual $\nu(A)$ with increasing excitation energy of the fissioning nucleus

It is well known that the shape of the excitation energy of fully accelerated fragments as a function of mass number $E^*(A)$ is reflected in the shapes of individual $\nu(A)$. At low and moderate En, both $E^*(A)$ and $\nu(A)$ exhibit sawtooth shapes. The behavior of $E^*(A)$ at high excitation energies of a fissioning nucleus sheds light on the $\nu(A)$ shape.

The sawtooth shape of $E^*(A)$ and $\nu(A)$ is due to the shell effects of the fragments. According to the TXE partition method of PbP, described in detail in Refs. [19,20], the dominant energy component is the available excitation energy at scission. This energy is partitioned between complementary nascent fragments under the assumptions of fragment level densities in the Fermi-gas regime and statistical equilibrium at scission, i.e., the available excitation energy at scission $E^*_{\rm sciss} = E^L_{\rm sciss} + E^H_{\rm sciss}$, is shared according to the ratio,

$$E^L_{\rm sciss}/E^H_{\rm sciss} = a^L_{\rm sciss}/a^H_{\rm sciss}, \tag{9}$$

in which the level-density parameters $a^{L,H}_{\rm sciss}$ are expressed by the superfluid formula,

$$a(A,Z,E^*) = \begin{cases} \tilde{a}(A)\left(1 + \frac{\delta W(A,Z)}{U^*}\{1 - \exp[-\gamma(A)U^*]\}\right), & U^* = E^* - E_{\rm cond}, \quad E^* > E_{\rm cr}, \\ a_{\rm cr} = \tilde{a}(A)\left(1 + \frac{\delta W(A,Z)}{E_{\rm cr}}\{1 - \exp[-\gamma(A)E_{\rm cr}]\}\right), & E^* \leqslant E_{\rm cr}. \end{cases} \tag{10}$$

In Eq. (10) the notation E^* means the excitation energies of the fragments $E^{L,H}_{\rm sciss}$ entering Eq. (9). The condensation energy is taken as $E_{\rm cond} = 3a_{\rm cr}\Delta^2/2\pi^2 - n\Delta$, where $a_{\rm cr}$ is the critical level-density parameter, $\Delta = 12/\sqrt{A}$ is the pairing correlation function, and $n = 0$, 1 and 2 for even-even, odd-A, and odd-odd nuclei, respectively. The critical temperature of the phase transition from superfluid (superconductive) to normal states is given by $t_{\rm cr} = 0.567\Delta$, and the critical energy is $E_{\rm cr} = a_{\rm cr}t^2_{\rm cr}$. δW is the shell correction, $\tilde{a}(A)$ is the asymptotic value of the level-density parameter (obtained when all shell effects are washed out), and $\gamma(A)$ is the parameter of the function defining the damping of the shell effects. Different shell corrections and parametrizations of the damping and the asymptotic level-density parameters can be used. In the present paper, as in the majority of PbP calculations, the parametrizations proposed by Ignatiuk [17] are used, i.e., $\tilde{a} = 0.073\,A + 0.115\,A^{2/3}$ and $\gamma = 0.4\,A^{-1/3}$.

The level-density parameters and excitation energies of complementary fragments at scission are obtained simultaneously by an iterative procedure according to Eqs. (9) and (10) under the condition of equal nuclear temperatures. The resulting level-density parameters at scission of the fragments corresponding to the first compound nucleus undergoing fission ^{239}U are plotted as a function of A in Fig. 12 at two incident neutron energies, a high one and a low one, i.e., $En = 80$ MeV (red circles) and $En = 2$ MeV (blue squares).

As it can be seen, at $En = 80$ MeV when the nascent fragments have high excitation energies, the shell effects [entering the superfluid expression of Eq. (10)] are almost completely attenuated. For a great part of the nascent fragments the level-density parameters (red circles) are very close to the asymptotic value $\tilde{a}$ plotted with a black dashed line, except for fragments with A around 130 (for which the shell corrections have large negative values due to the magic numbers $Z = 50$ and $N = 82$).

Details about the complete or incomplete damping of the shell effects, depending on the type of fragments (Z and N) and their energies resulting from the iterative procedure of

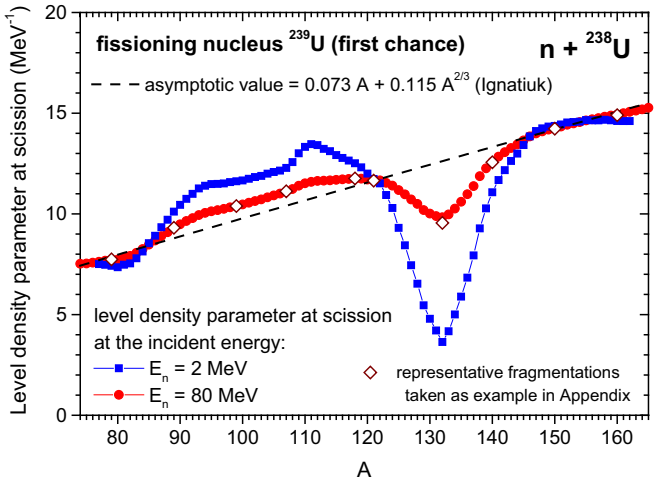

FIG. 12. Level-density parameter of the fragments at scission for the main fissioning nucleus ^{239}U in the $n + ^{238}$U reaction at $En = 80$ MeV (red circles) and $En = 2$ MeV (blue squares). The asymptotic level-density parameter is plotted with a black dashed line.

partition at scission are given in the Appendix (where five representative fragmentations of ^{239}U are discussed).

Consequently both, the excitation energies at scission and at full acceleration of the fragments corresponding to the main fissioning nucleus ^{239}U at $En = 80$ MeV, exhibit an almost linear increase over the A range of asymmetric fragmentations in which $A_H > 140$ and $A_L < 99$, see Fig. 13 and Fig. 17 of the Appendix. The visible deviation from linearity at A between approximately 109 and 130 are due to the presence of magic heavy fragments (with very pronounced negative shell corrections). Also the higher TXE values near symmetry (compared to the asymmetric region where TXE is almost constant) are reflected in an increase in the fragment excitation energies around $A = 120$.

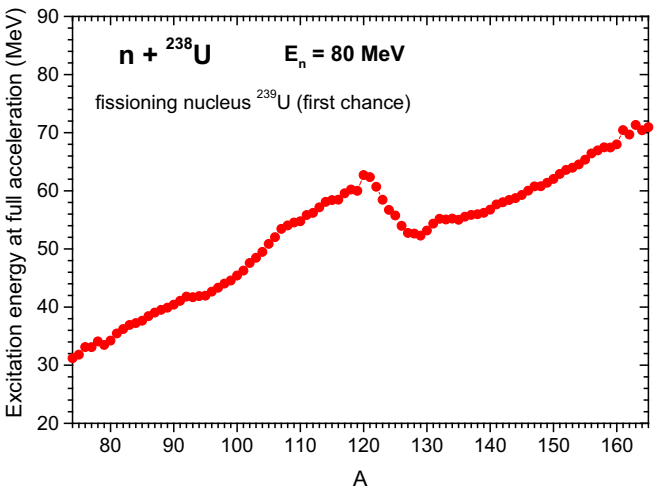

FIG. 13. Excitation energy of fully accelerated fragments of the main fissioning nucleus ^{239}U in the $n + ^{238}$U reaction at an incident neutron energy of 80 MeV.

The behaviour of $E^*(A)$ plotted in Fig. 13, exhibiting a disappearing sawtooth shape, is well reflected in the shape of the individual $\nu(A)$ of ^{239}U at $En = 80$ MeV plotted with open dark yellow squares in the right lower panel of Fig. 5.

It was observed (e.g., Refs. [34,35]) that the ratio $\nu_H/(\nu_L + \nu_H)$ as a function of A_H obtained from experimental $\nu(A)$ data (available at low fission energies, i.e., spontaneous fission and neutron-induced fission at incident energies below the second fission chance threshold) exhibits a systematic behavior. This behavior was well reproduced by the PbP results of $\nu(A)$ for many fissioning systems reported during time (starting with Ref. [36] up to recent papers, e.g., Refs [14,20].).

The shape of the fragment excitation energy ratio E^*_H/TXE at full acceleration resulting from the TXE partition method of PbP (Refs. [10,20] and references therein) is similar to the shape of the experimental $\nu_H/(\nu_L + \nu_H)$ as a function of A_H (see Ref. [14] and references therein).

At thermal and low En the systematic behavior of the ratios $\nu_H/(\nu_L + \nu_H)$ and E^*_H/TXE as a function of A_H consists of the following aspects: The ratio is less than 0.5 for fragmentations with A_H going from symmetric fission up to about 140 with a minimum placed at A_H around 130 (due to the magic or doubly magic heavy fragment $N = 82$, $Z = 50$). The ratio is of about 0.5 at A_H around 140 (i.e., the complementary fragments of the most probable fragmentations emit almost equal numbers of prompt neutrons), and it exhibits an almost linear increase for A_H above 140. The value of the minimum of this ratio placed at A_H around 130 is increasing with increasing En.

As we have mentioned in previous publications (e.g., Ref. [14] and references therein) these shapes of the ratios $\nu_H/(\nu_L + \nu_H)$ and E^*_H/TXE as a function of A_H at low En can be schematically approximated (parametrized) by linear segments. I.e., a segment connecting the value of 0.5 at symmetric fission with the minimum value at A_H around 130, followed by a segment connecting this minimum value with the value of about 0.5 at A_H around 140 and a last segment fitting the almost linear increase of these ratios at A_H above 140.

Such schematic representations corresponding to the fissioning nucleus ^{239}U at En below the second fission chance threshold, are qualitatively illustrated in Fig. 14 by the red solid and wine dashed lines.

Note, these lines can also reproduce in a qualitative way the behavior of the $\nu_H/(\nu_L + \nu_H)$ ratio of another fissioning nucleus with the same mass number, induced for instance by thermal neutrons and neutrons with En of about 4 MeV–5 MeV, respectively.

The other lines in Fig. 14 give a qualitative representation for the evolution of the $\nu_H/(\nu_L + \nu_H)$ shape with increasing excitation energy of the fissioning nucleus ^{239}U. The dark yellow dashed-double-dotted line corresponds to En values where a few fission chances are involved (e.g., En of about 18–25 MeV). The other lines are qualitative illustrations of the multiplicity ratio of the fissioning nucleus ^{239}U at En values where many fissioning nuclei of the main and secondary nucleus chains are involved, e.g., En of about 50 MeV (blue dashed-dotted line), of about 70 MeV (green dotted line), and 80 MeV (black line).

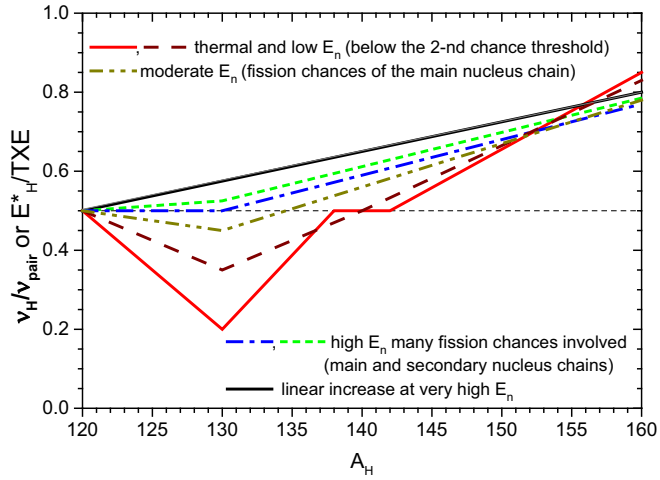

FIG. 14. A schematic representation of the systematic behavior of the ratio $\nu_H/\nu_{\rm pair}$ or E^*_H/TXE as a function of A_H at different excitation energies of the fissioning nucleus: going from excitation energies corresponding to *En* values below the second fission chance threshold (solid red line and wine dashed line) up to very high *En* (black line) when $E^*(A)$ and $\nu(A)$ exhibit a linear increase.

The schematic representation of the $\nu_H/(\nu_L+\nu_H)$ ratio by the black line in Fig. 14 is explained in Fig. 15 as follows. The individual $\nu(A)$ of ^{239}U at $En = 80$ MeV plotted in this figure with open black squares are fitted by the red line.

When $\nu(A)$ is taken linear, i.e., $\nu(A) = \alpha A + \beta$, the prompt neutron multiplicity of a mass pair ($A_L + A_H = A_0$) becomes constant (independent of A), i.e., $\nu_{\rm pair} = \alpha A_0 + 2\beta$, and obviously the $\nu_H/(\nu_L+\nu_H)$ ratio as a function of A_H becomes a line with the slope $\alpha/\nu_{\rm pair}$ and the intercept $\beta/\nu_{\rm pair}$. The linear fit of $\nu(A)$ plotted with a red line in Fig. 15 leads to $\nu_{\rm pair} = 10.203$ (dashed blue line in Fig. 15) approximating very well the calculated $\nu_{\rm pair}(A)$ (open gray

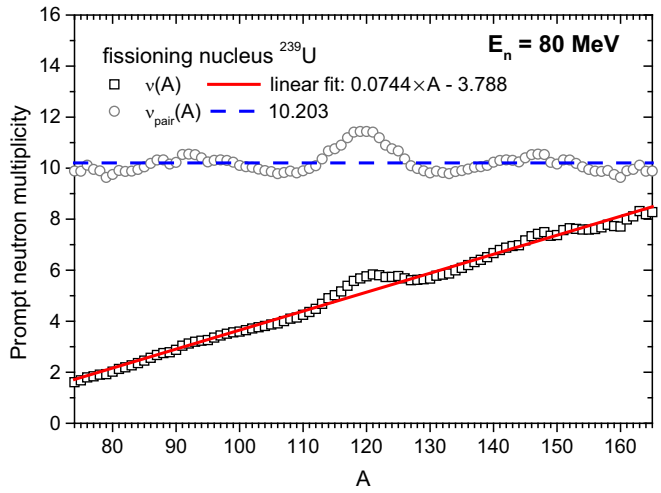

FIG. 15. The individual $\nu(A)$ of ^{239}U at $En = 80$ MeV is plotted with open black squares and its linear fit with a red line. The individual $\nu_{\rm pair}(A)$ is plotted with open gray circles. The constant $\nu_{\rm pair}$ value obtained by considering the linear fit of $\nu(A)$ is plotted with a dashed blue line.

circles) in the asymmetric fission region. The corresponding ratio $\nu_H/(\nu_L+\nu_H)$ is just the black line plotted in Fig. 14.

Note, Fig. 14 gives only a qualitative illustration by schematic linear representations of the change in shape of the ratio $\nu_H/(\nu_L+\nu_H)$ or E^*_H/TXE as a function of A_H for an individual fissioning nucleus with increasing excitation energy. In particular this evolution is interesting for the main fissioning nucleus (first fission chance).

The total $\nu(A)$ distribution (calculated according to Eq. (4) as a superposition of individual $\nu(A)$ weighted with the fission chance probabilities expressed as RF) could show a linear behavior over the entire A range maybe at much higher *En* when all individual $\nu(A)$ reach a linear shape (i.e., all calculated $\nu(A)$ can be well fitted by lines).

In other words this is happening when all fragments, coming from all compound nuclei (fission chances), have excitation energies high enough to wash out their shell effects, leading to the complete vanishing of the sawtooth shapes of all individual $\nu(A)$.

Looking at Fig. 6 and the lower right panel of Fig. 5, this trend of an almost linear increase of the total $\nu(A)$ can already be observed at $En = 80$ MeV.

IV. CONCLUSIONS

Data of post-neutron fragment distributions for ^{238}U at several tens of MeV incident energy were measured in a recent experiment at the LANSCE facility. To obtain the pre-neutron fragment distributions these data need the correction for prompt neutron emission. Consequently prompt neutron multiplicity distributions $\nu(A)$ at intermediate incident neutron energies are strongly required. The lack of experimental $\nu(A)$ data at incident neutron energies where multiple fission chances are involved imposes the use of models to predict $\nu(A)$.

The Point-by-Point model of prompt emission is able to provide the individual $\nu(A)$ distributions of the compound nuclei of the main and secondary nucleus chains that are undergoing fission at a given *En*. The total $\nu(A)$ are then obtained by averaging these individual $\nu(A)$ over the fission chance probabilities expressed as total and partial fission cross-section ratios.

The PbP calculations show that the sawtooth shapes of individual $\nu(A)$ become less pronounced with increasing excitation energy of the compound nuclei undergoing fission. At high incident neutron energies (e.g., of 70 and 80 MeV) the prompt neutron distributions $\nu(A)$ of the first few fissioning nuclei of the U and Pa chains, having the highest excitation energies, exhibit an almost linear increase. This shape is explained by the complete damping of shell effects in the superfluid expression of the level-density parameter of a great part of the fragments. This fact leads to a smooth and almost linear increase of the fragment excitation energy with the fragment mass number that is reflected in a smooth and almost linear behavior of individual $\nu(A)$.

An indirect validation of $\nu(A)$ is possible through the comparison of the calculated total average number of prompt neutrons with existing experimental data. This comparison can

be used as an indirect validation of predicted $\nu(A)$ because the magnitude of the average number of prompt neutrons coming from fragments $\langle\nu\rangle_{\rm FF}$ [obtained by averaging $\nu(A)$ over $Y(A)$] is strongly dependent on the $\nu(A)$ distribution and has only a weak dependence on the $Y(A)$ distribution.

The present $\nu(A)$ results averaged over available $Y(A)$ distributions (i.e., experimental $Y(A)$ measured at JRC-IRMM and $Y(A)$ provided by the GEF code) lead to total average prompt neutron numbers $\langle\nu\rangle_{\rm tot}$ in agreement with the experimental data.

The differences between the total $\nu(A)$ obtained by averaging the PbP results of individual $\nu(A)$ over fission cross-section ratios of different evaluations (e.g., ENDF/B-VII, JENDL4, and JEFF3.1) are almost insignificant.

A comparison of the present results with those provided by the GEF code is justified by the use of the $\nu(A)$ predicted by GEF to obtain the preliminary pre-neutron fragment data of ^{238}U(n,f) up to $En = 30$ MeV reported in Ref. [1].

This comparison revealed a much higher $\langle\nu\rangle_{\rm tot}$ of GEF than of PbP over the entire *En* range up to 80 MeV and significant differences between the $\nu(A)$ shapes of PbP and GEF at high *En*. The PbP results of $\nu(A)$ at high *En* reflect the influence of the almost linear shape of individual $\nu(A)$ corresponding to the first fissioning nuclei of the U and Pa chains. The $\nu(A)$ results of GEF at high *En* are deviating from this linear tendency.

The significant differences in shape and magnitude between the $\nu(A)$ predictions of PbP and GEF are expected to influence the recovered pre-neutron fragment mass distributions from post-neutron fragment data, that will be the subject of a future paper.

ACKNOWLEDGMENTS

One of the authors (A.T.) acknowledges a short-term visit support by the European Commission within the framework of the CHANDA program (agreement number 605203). A part of this work was done in the frame of the Romanian Exploratory Research Projects.

APPENDIX

At high excitation energy of a fissioning nucleus, e.g., the main compound nucleus ^{239}U at $En = 80$ MeV, the shell

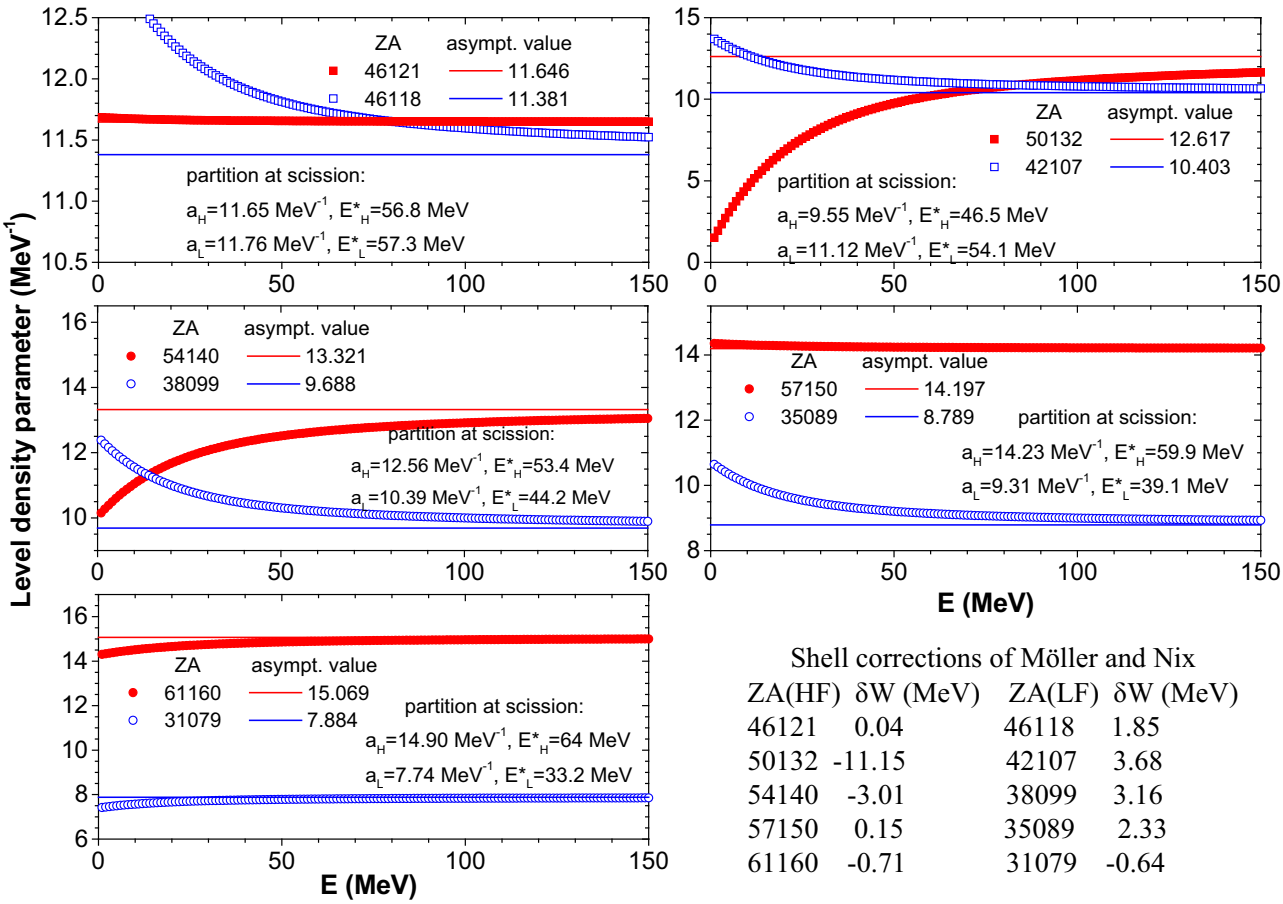

Shell corrections of Möller and Nix

ZA(HF)	δW (MeV)	ZA(LF)	δW (MeV)
46121	0.04	46118	1.85
50132	-11.15	42107	3.68
54140	-3.01	38099	3.16
57150	0.15	35089	2.33
61160	-0.71	31079	-0.64

FIG. 16. Level-density parameter of the superfluid model (using the Ignatiuk parametrizations of $\tilde{a}$ and γ [17]) as a function of fragment energy for five representative fragmentations of the fissioning nucleus ^{239}U. The level-density parameters of heavy fragments are plotted with full red circles, and those of the complementary light fragments are plotted with open blue circles. The asymptotic level-density parameters of heavy and light fragments are plotted with red and blue lines, respectively. The values of the level-density parameters and excitation energies at scission (for the case of $En = 80$ MeV) are given in the figure legends. The shell corrections of Möller and Nix [18] (entering the superfluid formula) are given in the lower right part.

effects of a great part of the nascent fragments are washed out, their level-density parameters reaching the asymptotic value $\tilde{a}$. But this is not happening for all fragments.

To demonstrate this fact, five representative fragmentations of the main fissioning nucleus ^{239}U are taken as examples, i.e., one near symmetry ($ZA_H = 46121$, $ZA_L = 46118$), one in which the heavy fragment is doubly magic ($ZA_H = 50132$, $ZA_L = 42107$), a very probable fragmentation ($ZA_H = 54140$, $ZA_L = 38099$), and two other very asymmetric fragmentations ($ZA_H = 57150$, $ZA_L = 35089$) and ($ZA_H = 61160$, $ZA_L = 31079$).

The level-density parameters of these representative fragments, calculated according to Eq. (10) are plotted as a function of E^* in Fig. 16 in separate panels for each fragmentation. The level-density parameters are plotted with full red circles for the heavy fragments and open blue circles for the complementary light ones. The asymptotic level-density parameters of heavy and light fragments are plotted with red and blue lines, respectively.

As it was mentioned in the main text, the level-density parameters and excitation energies of the complementary fragments at scission are obtained simultaneously by an iterative procedure according to Eqs. (9) and (10) (in which E^* is $E^{L,H}_{\rm sciss}$) under the condition of equal nuclear temperatures. They are given in the legends of Fig. 16.

As it can be seen for the near symmetric fragmentation (46121, 46118) the level-density parameters at scission of both fragments almost reach the asymptotic value. In the case of the fragmentation (50132, 42107) the level-density parameters are far from their asymptotic values, especially the double magic heavy fragment with a pronounced shell effect. For the fragmentation (54140, 38099), one of the most probable, again both fragment level-density parameters do not reach the asymptotic values. For the fragmentation (57150, 35089) only the level-density parameter at scission of the heavy fragment is close to the asymptotic value. In the case of the far asymmetric fragmentation (61160, 31079) both level-density parameters at scission are close to their asymptotic values. The level-density parameters at scission of these fragments are given with open diamonds in Fig. 12 of the main text.

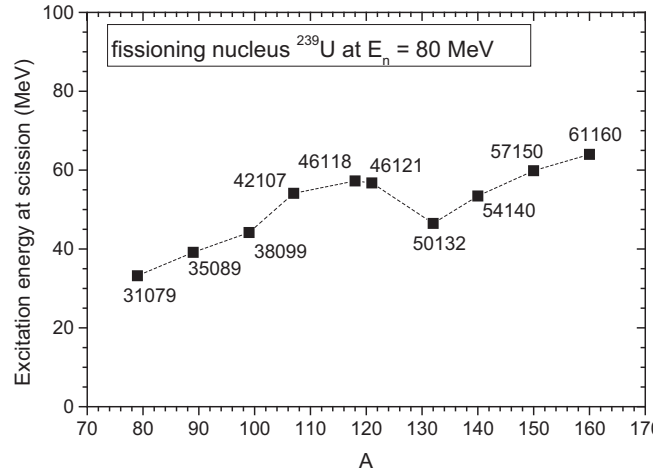

FIG. 17. Excitation energy at scission (resulting from the partition at scission under the condition of statistic equilibrium, i.e., equal nuclear temperature of complementary fragments) as a function of fragment mass for the fragments of five representative fragmentations of ^{239}U at $En = 80$ MeV. $ZA = 1000Z + A$ of the fragments are indicated in the figure.

The excitation energies at scission of the fragments entering the fragmentations discussed above are plotted as a function of fragment mass in Fig. 17. As can be seen the behavior of these energies is not linear.

[1] F.-J. Hambsch, A. Tudora, D. L. Duke, and F. Tovesson, *International Conference PHYSOR "Unified Theory and Experiments in the 21st Century"*, Sun Valley, ID, 2016 (American Nuclear Society, La Grange Park, IL, 2016).

[2] J. P. Lestone, Nucl. Data Sheets **112**, 3120 (2011).

[3] K.-H. Schmidt and B. Jurado, GEFcode version 2014/2.1, available online http://www.cenbg.in2p3.fr/-GEF-; http://www.khs-erzhausen.de/GEF.html.

[4] K.-H. Schmidt and B. Jurado, GEFcode version 2015/2.2, available online http://www.cenbg.in2p3.fr/-GEF-; http://www.khs-erzhausen.de/GEF.html.

[5] K.-H. Schmidt, B. Jurado, C. Amouroux, and C. Schmitt, Nucl. Data Sheets **131**, 107 (2016).

[6] J. S. Fraser and J. C. Milton, Phys. Rev. **93**, 818 (1954).

[7] R. Müller, A. A. Naqvi, F. F. Käppeler, and F. Dickmann, Phys. Rev. C **29**, 885(1984).

[8] A. A. Naqvi, F. F. Käppeler, F. Dickmann, and R. Müller, Phys. Rev. C **34**, 218 (1986).

[9] R. Vanderbosh and J. R. Huizenga, *Nuclear Fission* (Academic, New York/London, 1973).

[10] R. Capote, Y. J. Chen, F.-J. Hambsch, N. Kornilov, J. P. Lestone, O. Litaize, B. Morillon, D. Neudecker, S. Oberstedt, N. Otuka, V. G. Pronyaev, A. Saxena, O. Serot, O. A. Scherbakov, N. C. Shu, D. L. Smith, P. Talou, A. Trkov, A. C. Tudora, R. Vogt, and A. S. Vorobyev, Nucl. Data Sheets **131**, 1 (2016).

[11] A. Tudora, G. Vladuca, and B. Morillon, Nucl. Phys. A **740**, 33 (2004).

[12] A. Al-Adili, F.-J. Hambsch, S. Pomp, and S. Oberstedt, Phys. Rev. C **86**, 054601 (2012).

[13] Evaluated Nuclear Data File JEFF3.2 (2014), original data taken from JEFF3.1.1 (CEA/DAM), files ZA = 092238, MF = 3, MT = 18, 19, 20, 21, 38. Available online https://www-nds.iaea.org.

[14] A. Tudora, F.-J. Hambsch, S. Oberstedt, G. Giubega, and I. Visan, Nucl. Sci. Eng. **181**, 289 (2015).

[15] O. Bersillon, computer code SCAT2, OECD-NEA-DB-CPS, package NEA-0859/07, version 2011.

[16] Reference Input Parameter Library RIPL3 (2009), Segment =, Optical Parameterizations, Becchetti-Greenless potential IREF = 100. Available online https://www-nds.iaea.org.

[17] A. Ignatiuk in *Reference Input Parameter Library RIPL1 Handbook for Calculations of Nuclear Reaction Data*, TECDOC-1034 (1998), Segment V, Chap. 5.1.4.
[18] RIPL3 Reference Input Parameter Library (2009), Segment Masses and Deformations, database of Möller and Nix. Available online https://www-nds.iaea.org.
[19] C. Morariu, A. Tudora, F.-J. Hambsch, S. Oberstedt, and C. Manailescu, J. Phys.G: Nucl. Part. Phys. **39**, 055103 (2012).
[20] A. Tudora, F.-J. Hambsch, I. Visan, and G. Giubega, Nucl. Phys. A **940**, 242 (2015).
[21] RIPL3 Reference Input Parameter Library (2009), Segment Masses and Deformations, database of Audi and Wapstra. Available online https://www-nds.iaea.org.
[22] Experimental nuclear data library EXFOR, all entries corresponding to the following identifiers: target: ^{238}U, reaction (n,f), quantity MFQ / Prompt neutron yield (nu-bar). Available online https://www-nds.iaea.org.
[23] J. Taieb, T. Granier, T. Ethvignot, M. Devlin, R. C. Haight, R. O. Nelson, J. N. O'Donnell, and D. Rochman, 2007, EXFOR library, entry 14215001. Available online https://www-nds.iaea.org.
[24] T. Ethvignot, M. Devlin, H. Duarte, T. Granier, R. C. Haight, B. Morillon, R. O. Nelson, J. M. O'Donnell, and D. Rochman, Phys. Rev. Lett. **94**, 052701 (2005).
[25] B. Laurent, T. Granier, G. Bélier, A. Chatillon, J.-F. Martin, J. Taieb, F.-J. Hambsch, F. Tovesson, A. B. Laptev, R. C. Haight, R. O. Nelson, and J. M. O'Donnell, Nucl. Instrum. Methods Phys. Res., Sect. A **745**, 99 (2014).
[26] A. Tudora, F.-J. Hambsch, and S. Oberstedt, Nucl. Phys. A **890-891**, 77 (2012)
[27] E. Birgersson, A. Oberstedt, S. Oberstedt, and F.-J. Hambsch, Nucl. Phys. A **817**, 1 (2009).
[28] F. Vivès, F.-J. Hambsch, H. Bax, and S. Oberstedt, Nucl. Phys. A **662**, 63 (2000).
[29] A. Tudora, Nucl. Phys. A **916**, 79 (2013).
[30] A. Tudora, F-J. Hambsch, and S. Oberstedt, Nucl. Phys. A **917**, 43 (2013).
[31] J. O. Denschlag, M. C. Duijvestijn, Th. Ethvignot, F.-J. Hambsch, J. Katakura, Yu. V. Kibkalo, M. Lammer, Liu Tingjin, V. M. Maslov, R. W. Mills, A. C. Wahl, and S. V. Zhdanov, *Fission Product Yield Data for the Transmutation of Minor Actinide Nuclear Waste*, IAEA STI/PUB/1286 (IAEA, Vienna, 2008), Chap. 4.2 (A.C.Wahl), pp. 117–148.
[32] Evaluated Nuclear Data File ENDF/B-VII (2011), files ZA = 092238, MF = 3, MT = 18, 19, 20, 21, 38. Available online https://www-nds.iaea.org.
[33] Evaluated Nuclear Data File JENDL4 (2012), files ZA = 092238, MF = 3, MT = 18, 19, 20, 21, 38. Available online https://www-nds.iaea.org.
[34] A. C. Wahl, At. Data Nucl. Data Tables **39**, 1 (1988).
[35] C. Manailescu, A. Tudora, F.-J. Hambsch, C. Morariu, and S. Oberstedt, Nucl. Phys. A **867**, 12 (2011).
[36] A. Tudora, Ann. Nucl. Energy **33**, 1030 (2006).